

**WAVEFRONT ENGINEERING FOR
MANIPULATING LIGHT-ATOM INTERACTIONS**

YEO XI JIE

A0140239M

e0004149@u.nus.edu

Report submitted to

Department of Physics, National University of Singapore

in partial fulfilment for the module

PC3288/PC3289 ADVANCED UROPS IN PHYSICS I/II

November 2017

Contents

1	Manipulations of Wavefronts	5
1.1	Motivations	5
1.2	The Spatial Light Modulator (SLM)	5
1.3	Controlling the SLM	8
1.3.1	The Meadowlark XY Series SLM (P512L)	8
1.3.2	Basic Concepts	10
1.3.3	Display Configurations	10
1.3.4	Controlling Phase Shifts with an Image	10
2	Simple Applications of the SLM	15
2.1	Characterising Phase Shifts of the SLM	15
2.1.1	Background of Experiment	15
2.1.2	Implementation	16
2.2	Beam Displacement by Blazed Grating	20
2.3	Beam Position Measurements	24
2.3.1	Method A: Using the birefringence of the SLM	24
2.3.2	Method B: Fashioning the SLM as a Knife Edge	26
2.4	Creating Laguerre-Gaussian Mode Beams	29
3	Measuring Wavefronts	33

3.1	Hartmann-Shack Wavefront Sensor	33
3.1.1	How it Works	34
3.1.2	A Note on the Lenslet Array	35
3.2	Zernike Modes	36
4	Effect of Wavefront Corrections on Fiber Coupling	38
5	Conclusion	44
5.1	Future Outlook	44

Acknowledgements

First, I would like to thank Christian Kurtsiefer for giving me the opportunity to work in his group for this project. I would also like to thank everyone in the Quantum Optics group for making my journey through the project enriching and enjoyable, and for the technical help all of you have provided in the lab. A special mention to my mentors Matthias Steiner and Wilson, for their tireless effort and patience in giving me guidance and direction for the project, as well as support in the laboratory, and also to Chang Hoong, for the collaboration in the later part of the project and the effort for the countless number of times we rebuilt the setup while debugging faults.

To my loved ones and friends, thank you for understanding the less time spent with you all in order to complete this project.

Abstract

We aim to control and enhance the interaction between single atoms and light by fine tuning the wavefront of the incident beam. To manipulate the wavefront, we use a Spatial Light Modulator (SLM). Here I report experiments that were done to characterise the SLM, understanding the workings of the Hartmann-Shack sensor (a tool for measuring wavefronts), and show how the SLM improves the coupling efficiency of light through an optical fiber.

Chapter 1

Manipulations of Wavefronts

1.1 Motivations

A photon-atom interface plays an important role in many quantum information protocols [1, 2]. A promising method to achieve strong photon-atom interaction is to focus the incident light strongly onto the atom [3]. However, we encounter a serious problem when implementing this idea in the laboratory. The real lenses that we use are not ideal lenses as the aberrations of the focusing optics leads to weaker foci and weak light-atom interaction [4, 5]. Our idea is to tune the wavefront of the incident beam in such a way that it pre-compensates for the aberrations of the focusing optics. In order to tune the wavefront of the incident beam, we make use of a device known as a spatial light modulator (SLM). Hence, it is important to understand how the SLM works, and how to operate it. This chapter introduces the workings of the SLM in general and the specific operation technique for our model of the SLM.

1.2 The Spatial Light Modulator (SLM)

Today, there are many types of SLMs commercially available. Some come in the form of deformable mirrors and some using liquid crystal based technologies [6, 7]. The SLM can be

a reflective type (with the modulated light reflecting off its surface) or the transmissive type (with the modulated light transmitted through the SLM instead) [8].

We discuss the reflective, liquid crystal type as that is the type of SLM that we are working with.

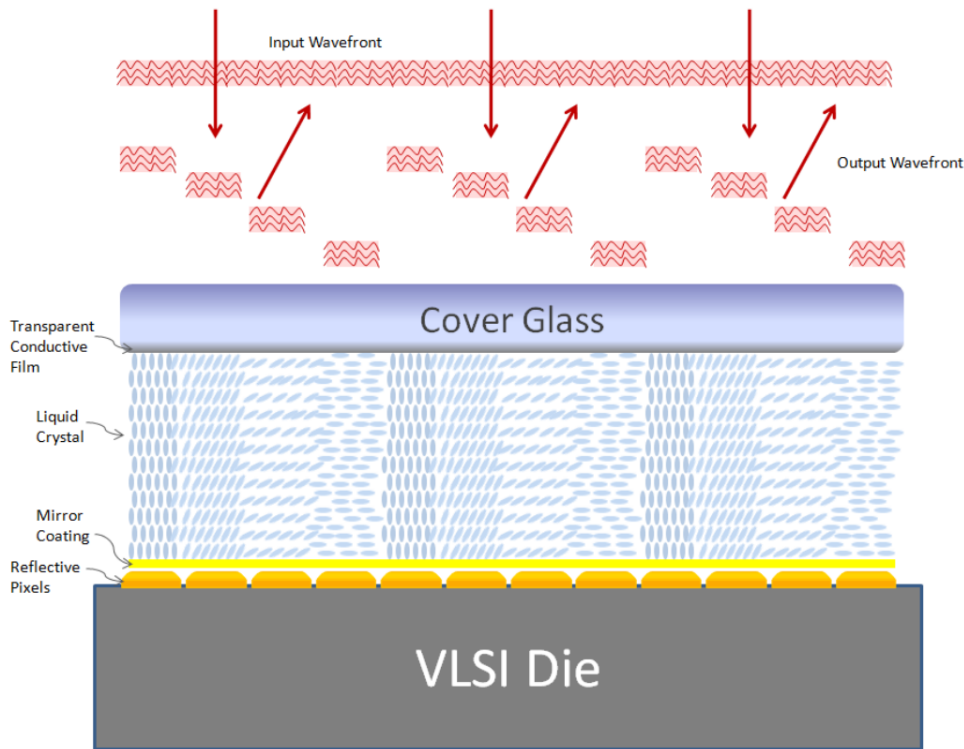


Figure 1.1: The cross section of the SLM [9]

Figure 1.1 shows a cross section of the SLM. The light that we send to the SLM comes in from the top of the diagram, and travels through the cover glass, the transparent conductive film, the liquid crystal array, before being back reflected by the pixel electrodes [9]. When a voltage is applied to the pixel electrode, an electric field is created between the cover glass of the SLM and the pixel electrode. Due to the presence of permanent dipoles in the liquid crystal molecules, the presence of an electric field changes the orientation of the liquid crystal molecules in between.

As the liquid crystals that are used in our SLM are nematic, the array of liquid crystals

align in a way that the long axes of the crystals are parallel to each other [10]. Thus, when an electric field is created between the coverglass and the pixel electrodes, the interaction between the dipole in the liquid crystal and the electric field will result in the rotation of the liquid crystal. This forms an angle between the coverglass and the long axes of the liquid crystal. However, due to the nematic nature of the liquid crystals, the liquid crystals will still be parallel to one another while being orientated at an angle between the coverglass and long axes of the crystal. Furthermore, as the refractive index of the liquid crystals is dependent on the orientation of the crystals, the refractive index of the liquid crystal at each pixel is manipulated by applying a suitable voltage at the electrode [11].

From Figure 1.2, we can see how the orientation of the liquid crystal is parallel to coverglass when no voltage is applied, and perpendicular to the coverglass when the maximal voltage is applied. For our SLM, the changes to the orientation of the liquid crystal by the voltages applied only affects the refractive index of horizontally polarised light, while the vertically polarised light remains unaffected.

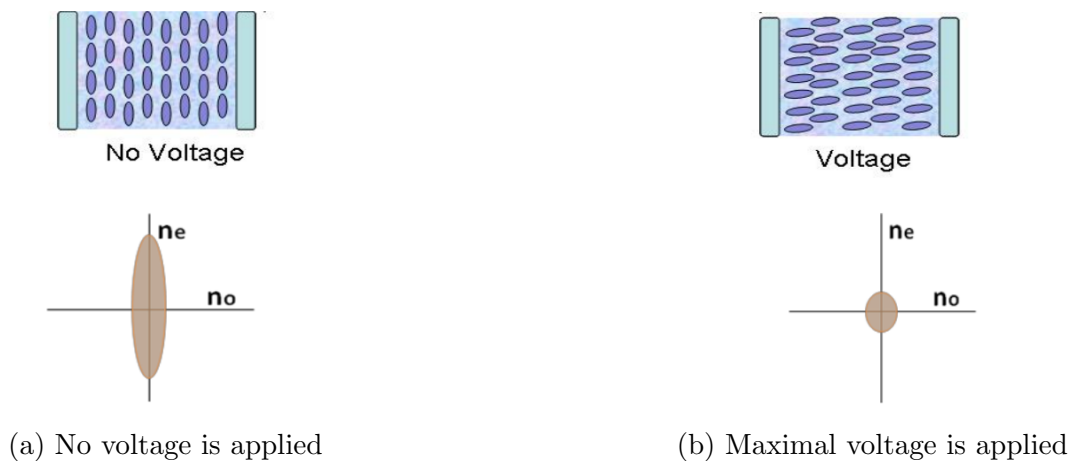


Figure 1.2: Orientation of liquid crystal with respect to coverglass and backplate (the vertical blue bars) in a bird's eye view of the optical table, and the corresponding distribution of the refractive index. n_e is the refractive index that affects horizontally polarised light and n_o is the refractive index that affects vertically polarised light. [9]

1.3 Controlling the SLM

1.3.1 The Meadowlark XY Series SLM (P512L)

Our SLM, the Meadowlark XY Series SLM (P512L), is shown in Figure 1.3a, along with a driver (Figure 1.3b) that acts as our interface to control the SLM. See Figure 1.4 for the technical specifications of the device.



(a) Spatial Light Modulator (not in operation)



(b) SLM Driver

Figure 1.3: The main components of the entire SLM device. The blue ribbon of the driver connects to an op-amp board(not shown) which sends the relevant pixel information via the brown ribbon that is connected to the SLM itself.

Large 512 x 512 Spatial Light Modulator	
Standard Design Wavelengths	532, 635, 785, 1064, & 1550 nm
Array Size	12.8 x 12.8 mm
Zero-Order Diffraction Efficiency	88% (maximum)
External Window	AR coated, $R_{avg} < 1.25\% @ \lambda$
Fill Factor (standard)	0.96
Format	512 x 512 (262,144 active pixels)
Phase Stroke (Double Pass)	$2\pi @ \lambda$
Pixel Pitch	25 x 25 μm
Phase Ripple	As low as 0.1%, based on SLM configuration
Reflected Wavefront Distortion (RMS Calibrated)	$\lambda/7 - \lambda/12$
Liquid Crystal Response Time, 10-90% (Standard)	30 - 100 ms
Maximum Liquid Crystal Switching Frequency (Standard)	10 - 33 Hz
Liquid Crystal Response Time, 10-90% (Hi-Speed)	2 - 15 ms
Maximum Liquid Crystal Switching Frequency (Hi-Speed)	67 - 500 Hz

Figure 1.4: The technical specifications for our SLM. Note: Our SLM is designed for 785 nm wavelengths. [12]

1.3.2 Basic Concepts

In essence, how we control our SLM is similar to how one uses a secondary computer monitor. The SLM is connected to the computer via a HDMI or DVI cable to the appropriate graphics output of the computer. We then “display” a full-screen image on the SLM (which is configured as the secondary monitor), which performs appropriate phase shifts on the SLM based on the information provided in the uploaded image.

1.3.3 Display Configurations

The physical “display” resolution of the Meadowlark XY Series SLM is 512 by 512, although the allowed display resolution configuration by the SLM graphics driver is 800 by 600 or 1024 by 768. As such, the effective region of the uploaded image where the SLM gets the phase shift information is only the top left 512 by 512 pixels. We take the 512 by 512 image that we want to use, and add black borders to it such that the resultant image matches the configured resolution for the display. This avoids scaling or stretching of the image, and each pixel of the SLM receives the correct information and performs the appropriate phase shift.

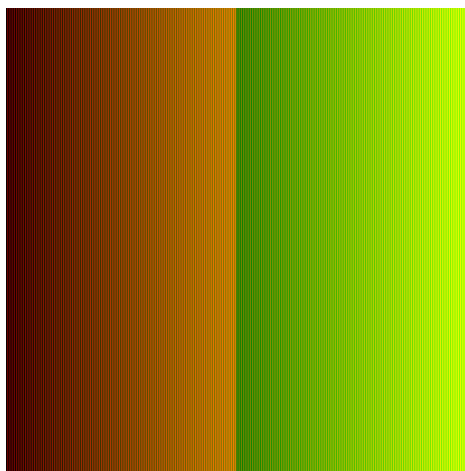
1.3.4 Controlling Phase Shifts with an Image

The phase shift each pixel can perform ranges from 0 - 2π . The amount of phase shift for each pixel on the SLM is determined by the colour of its corresponding pixel on the uploaded image. The format of the image that we use is a .BMP format and in this format, the colour of each pixel is determined by 24 bits (8 bits each for each channel of the primary colours: red, green and blue). In computing terminology, 8 bit of binary data allows us to set an integer between 0 - 255. This means that for each pixel in a typical .BMP image, the amount of each colour can be set with 0 being the setting for the absence of that colour, and 255 being the maximum amount of that colour in the pixel.

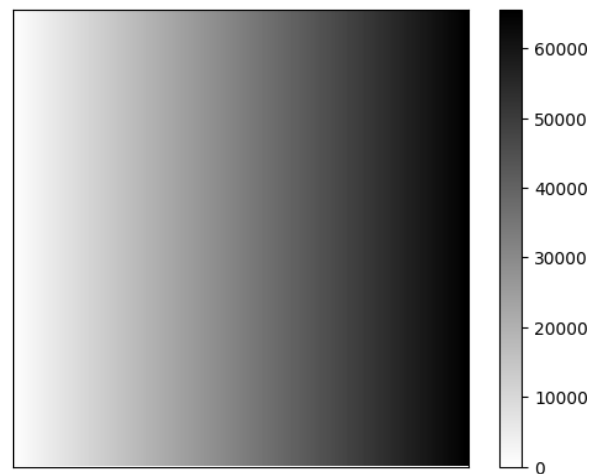
For our SLM, only the red and green channels of the image are used, which means the

uploaded image does not contain any blue. As a result, the range of the phase shift 0 to 2π is encoded into 16 bits of binary data (dividing the 2π to a range 0 to 65535), with 8 bits each contributed by the red and green channel. The 8 bits in the green channel are the most significant bits and the red channel has the least significant bits [9]. Thus, an uploaded image with no phase shifts, is black (due to an absence of green and red, and of course blue), whereas an image with 2π is yellow.

In order for us to visualise better how the phase shifts are performed on the SLM, I have written a software that converts the image we upload onto the SLM, to a 2-D plot that shows the phase shifts performed across the SLM. An example is shown in Figure 1.5, demonstrating the difficulty in interpreting the uploaded image to the relative phase shifts performed throughout the surface. Just by looking at Figure 1.5a, one cannot immediately tell that it is actually doing a linear phase shift pattern from 0 to 2π from the left to the right of the SLM.



(a) Phase shift information image (without black borders)

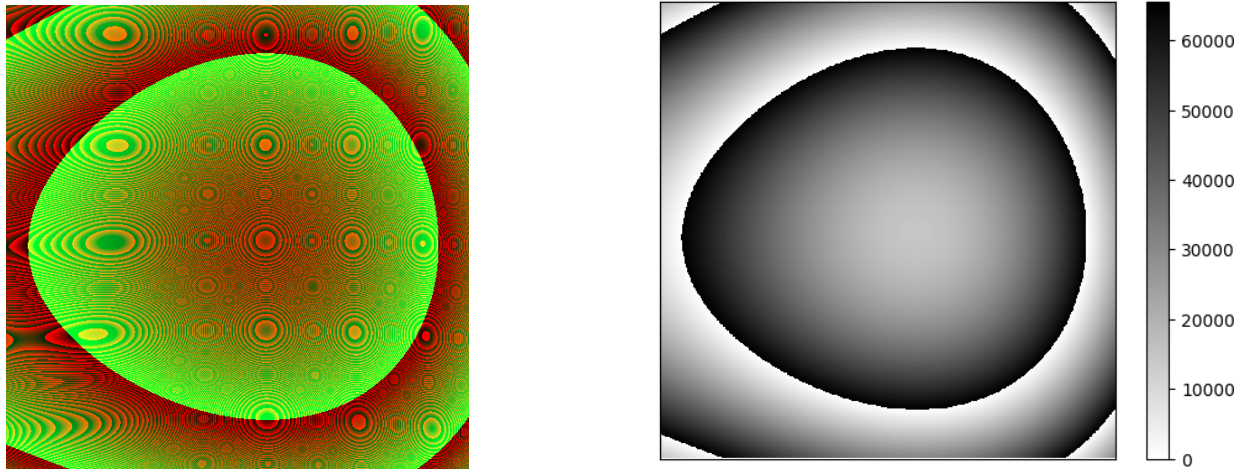


(b) Visualisation of Phase shift for Image

Figure 1.5: (a) An image which applies a linear increment of phase shift from the left to right across the SLM (b) The corresponding phase shift visualisation for the image in (a) with the heatmap showing the amount of phase shift in terms of the pixel's bit value ($0 - 65535$).

Wavefront Correction Image

The SLM is not flat, which results in non-uniform phase shifts even if a monochromatic image is uploaded to the SLM. To compensate for this offset, the manufacturer provides us with a Wavefront Correction Image specific for our device. When this image is uploaded, the relative phase difference across the entire surface of the SLM is 0. An example of such a correction image can be seen in Figure 1.6



(a) Factory provided Wavefront Correction Image (Without black borders)

(b) Visualisation of Phase shift

Figure 1.6: (a) An example of a wavefront correction image provided by factory that we upload onto the SLM for a uniform 0 phase shift (zero-phase shift image) (b) The corresponding phase shift visualisation for the image in (a) with the heatmap showing the amount of phase shift in terms of the pixel value (0 - 65535). The boundaries that sharply changes from black to white as the amount of phase shift starts from 0 after reaching 65535.

Lookup Table

Another key feature in the implementation of phase shifts using the SLM is the Lookup Table. The amount of phase shift for each pixel is determined by a 16 bit value taken from the green and red channels of the corresponding pixel in the uploaded .BMP image. However, again due to the calibration of the SLM, there is a mapping required between the phase shift we want for a pixel (set as a 16 bit value) to the actual value of that pixel to be sent to the SLM. This

mapping rule is customised for each individual SLM via a Lookup Table which maps the 16 bit value of the phase shift that we intend to perform at that pixel on the SLM to an appropriate output pixel value to be sent to the SLM. Thus, the image containing the information of the phase shifts to be performed has to be post-processed using the Lookup Table.

An example of the mapping between the phase shift we want and the post processed pixel by the Lookup Table can be seen in Figure 1.7, while a comparison between a post processed image with the original image can be seen in Figure 1.8.

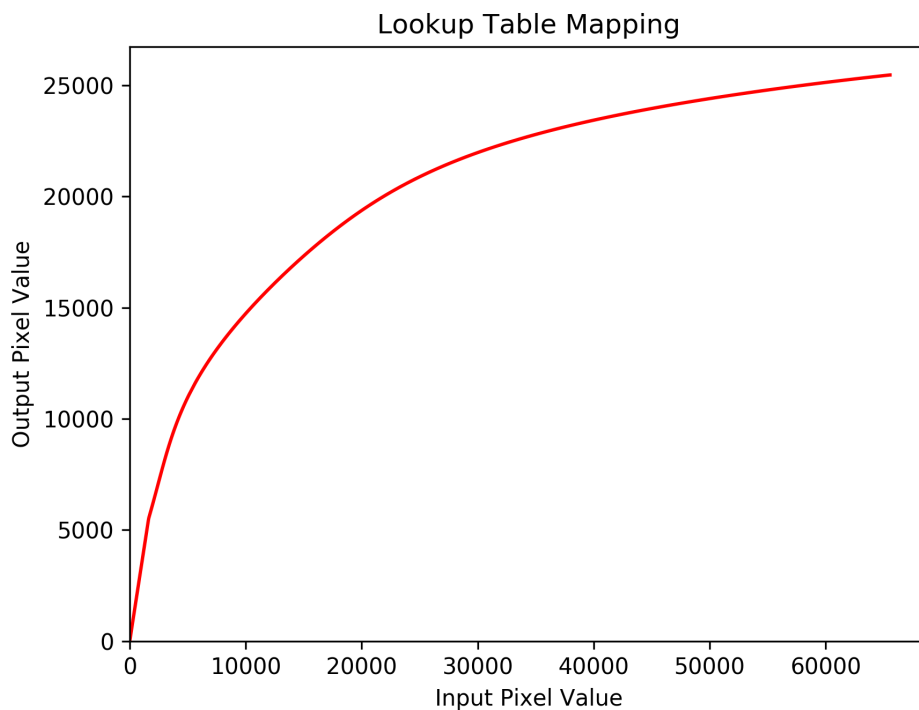
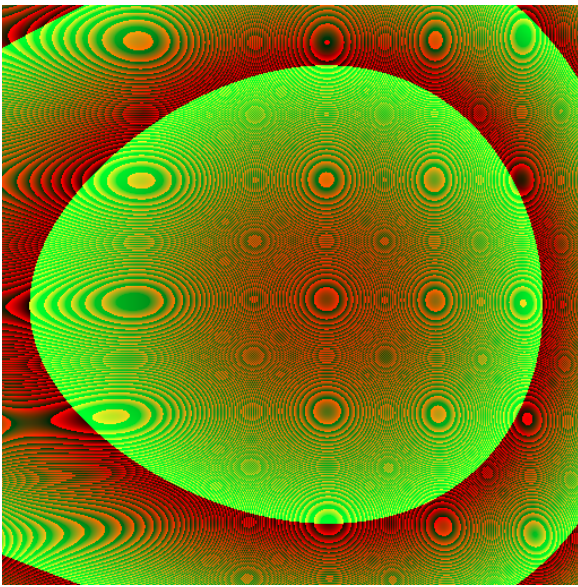
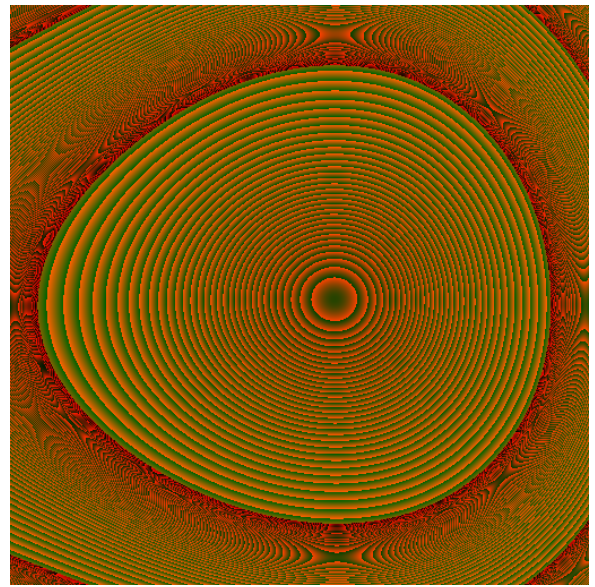


Figure 1.7: A plot of the input pixel value mapped to the output pixel value.



(a) Before Lookup Table Correction



(b) After Lookup Table Correction

Figure 1.8: (a) The wavefront correction image. (b) The wavefront correction image after being processed by the Lookup Table

Chapter 2

Simple Applications of the SLM

In the initial stages of familiarising with the SLM, we conducted some tests to demonstrate some capabilities of the SLM, and verify that the device is working as expected.

2.1 Characterising Phase Shifts of the SLM

First we characterise the phase shifts on the SLM; to test whether the device gives the proper phase shift as specified by the uploaded image. This is of utmost priority as this defines the functionality of the SLM.

In essence, we exploit the birefringence property of the SLM in order to transform it into a waveplate of variable relative phase (ϕ) between the horizontal and vertical polarisation of incident light on the SLM. Using the SLM as a waveplate allows us to change the polarization of the reflected light and do appropriate polarisation measurements thereafter.

2.1.1 Background of Experiment

The relative phase created between the horizontal and vertical polarisation by a generic waveplate is described by the following equation:

$$\phi = \frac{2\pi\Delta nL}{\lambda_0} \quad (2.1.1)$$

where ϕ is our relative phase, Δn is the difference in the refractive index between the ordinary axis and extra-ordinary axis, L is the total path length travelled by the light wave in the SLM and λ_0 is the wavelength of light in vacuum.

Since our SLM uses a change in the refractive index of our liquid crystal to perform the phase shifts, the variable that affects the relative phase shift between the horizontal and vertical polarisation is the difference in refractive index Δn . In our case, Δn is the difference in the refractive index between the variable refractive index in the horizontal polarisation and the constant refractive index in the vertical polarisation. This allows us to change the polarisation of a diagonally polarised beam incident on the SLM. We then measure the effects of phase shifts performed by the SLM with the help of a polarising beam splitter.

2.1.2 Implementation

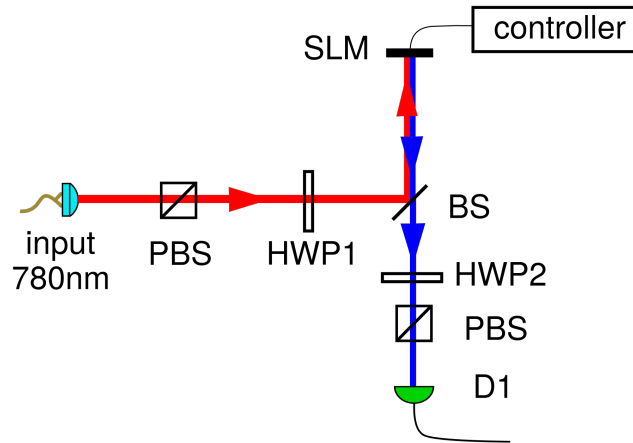


Figure 2.1: Setup used to do the phase shift measurement

Referring to Figure 2.1, we pass a horizontally polarised beam to a halfwave plate (HWP1)

which rotates the polarisation vector by 45° . The beam is then reflected off the SLM and passes through another half-wave plate (HWP2) that rotates the polarisation vector by -45° . Thereafter, the beam is passed into a polarising beam splitter (PBS), and we measure the intensity of the transmitted light with respect to the value of the uniform phase shift we have selected to upload with detector D1. The mathematical description of theory to the experiment is as follows:

In the basis of horizontal polarisation $|H\rangle$ and vertical polarisation $|V\rangle$ we denote:

$$|H\rangle \rightarrow \begin{bmatrix} 1 \\ 0 \end{bmatrix}, \quad |V\rangle \rightarrow \begin{bmatrix} 0 \\ 1 \end{bmatrix}$$

The operator for the half-wave plate rotated to an angle $\hat{H}(\theta)$ is:

$$\hat{H}(\theta) \rightarrow \begin{bmatrix} \cos \theta & \sin \theta \\ \sin \theta & -\cos \theta \end{bmatrix}$$

For an SLM that performs a uniform phase shift ϕ , the operator that transforms a $\hat{S}(\phi)$ is:

$$\hat{S}(\phi) \rightarrow \begin{bmatrix} e^{i\phi} & 0 \\ 0 & 1 \end{bmatrix}$$

with ϕ being taken from the Equation 2.1.1

As a result, if the horizontally polarised light that enters HWP1 has a state $|\psi\rangle = |H\rangle$, we measure the normalised intensity ($I(\phi)$) at D1 (as a function of the SLM phase shift ϕ) to be:

$$\begin{aligned} I(\phi) &= I_{max} \left| \frac{1}{\sqrt{2}} \langle H | \hat{H}(-45^\circ) \hat{S}(\phi) \hat{H}(45^\circ) | \psi \rangle \right|^2 \\ &= \frac{I_{max}}{2} (1 - \cos \phi) \end{aligned} \tag{2.1.2}$$

where I_{max} is the maximum intensity measured.

We measure the intensity of the light at D1 with a photodiode. The voltage measured across the resistor in the photodiode is proportional to the intensity. We recorded the data of how this voltage varied with the phase shift value of the uploaded image (in terms of bits) and fitted to the following function:

$$V(\phi_{bit}) = \frac{V_{max}}{2} \left(1 - \cos \left(\frac{2\pi}{\lambda} (\phi_{bit} - \phi_0) \right) \right) \quad (2.1.3)$$

where ϕ_{bit} is the phase shift value of the uploaded image, V is the voltage measured at photodiode, V_{max} is the maximum voltage measured, with the free fit parameters being the phase offset ϕ_0 , and the periodicity λ . Values of ϕ and λ in Equation 2.1.3 are in terms of bits.

From the fitting function, we obtain $\lambda = 63516 \pm 169$ $\phi_0 = 19886 \pm 60$. The non-zero value of ϕ_0 tells us that there is a difference in refractive index for horizontal polarisation light and vertical polarisation light even when no phase shift is applied to the SLM. We attribute the discrepancy of λ with the actual value of 65535 as the SLM is designed for use with 785nm light while we used 780nm light. The plot of the data is shown in Figure 2.2.

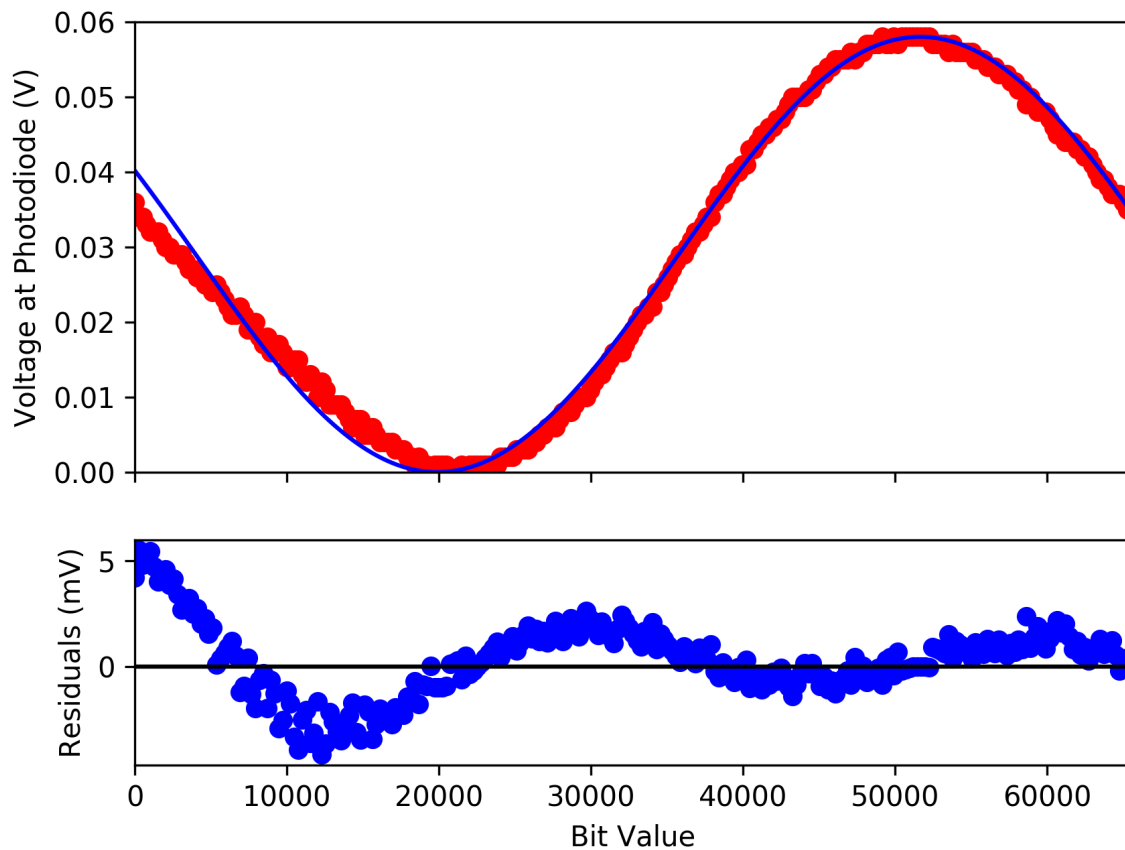


Figure 2.2: A plot of the voltage measured across the resistor at the photodetector (D1) against the value of the uniform phase shift (in bits) uploaded with the residuals shown in the bottom graph. From Figure 1.7, we see that the mapping function rises sharply for smaller input bit values and becomes more gentle when the input bit value is larger. We believe this results in our residuals in the above plot being larger in magnitude for small bit values and becoming smaller for larger bit values.

2.2 Beam Displacement by Blazed Grating

After knowing that uniform phase shifts can be performed as expected, we tested the performance of the SLM using a simple phase shift pattern. For this, we choose to use a blazed grating pattern because it is easy to implement due to its periodicity and we do not need to know the position of the beam on the SLM for it to work.

The blazed grating function used is as follows:

$$\phi(x) = \frac{2\pi}{\Lambda_x} x \pmod{2\pi} \quad (2.2.1)$$

where ϕ is the phase shift applied at position x on the SLM, and Λ_x is the periodicity (in pixels) of the grating in the x direction.

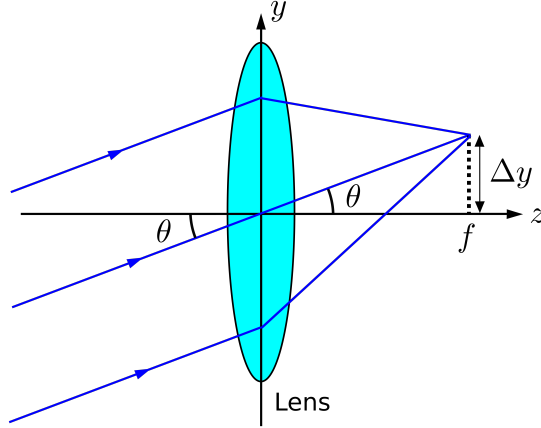


Figure 2.3: A diagram of the displacement of the focal point on the focal plane.

In essence, the blazed grating pattern steers the direction of the propagation of the wavefront of light by an angle $\theta \approx \lambda/\Lambda_x$ from its initial direction where λ is the wavelength of the light. We justify the use of the small angle approximation $\tan \theta \approx \theta$ as $\lambda \ll \Lambda_x$. Referring to Figure 2.3, we work out the trigonometry and show that this steering of the wavefront propagation by an angle θ results in a displacement of the focal point at the focal plane by an amount $d = f\lambda/\Lambda_x$ from the paraxial focus when the beam is passed through the converging lens, where f is the focal length of the lens used. We investigate the relationship between the beam displacement

(d) and Λ_x by constructing the setup shown in Figure 2.4.

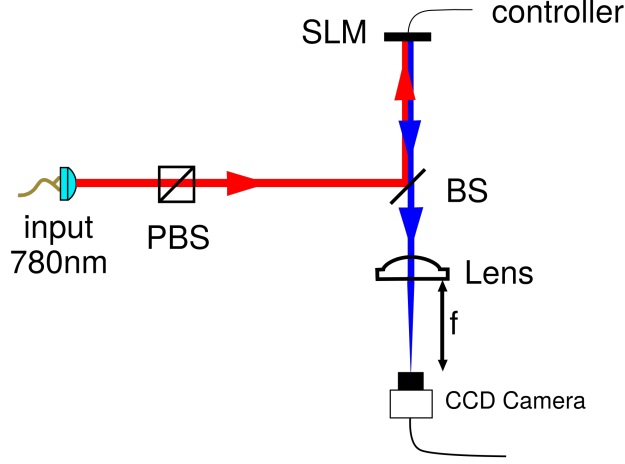


Figure 2.4: Setup to measure the displacement of the beam.

We took the images for different values of Λ_x (both positive and negative), and analysed the displacement of the beam on the camera. The data is then fit to the function:

$$d = k/\Lambda_x \quad (2.2.2)$$

where d being the beam displacement and the free parameter being k , where theoretically, $k = f\lambda$. The results of the fit can be seen in Figure 2.5.

Figure 2.6 shows some negatives of the images captured by our camera during the experiment. The recorded beam displacement fit well to an expected inverse relationship between the displacement d and the pixel width of the grating Λ_x . However, as the fit value of k ($1.20 \pm 0.03\text{mm} \cdot \text{px}$) in Equation 2.2.2 is smaller by a factor of 2.588 times from the theoretical value of k ($3.12\text{mm} \cdot \text{px}$), further investigations needs to be conducted.

With reference to Figure 2.6, we compare the intensity of the displaced beam (highlighted by the rectangle) and the intensity of the remnant spots (highlighted by our circle) using the images captured and calculate the average diffraction efficiency to be $91 \pm 3\%$.

From this experiment, we also note that when we use phase shift patterns with a small

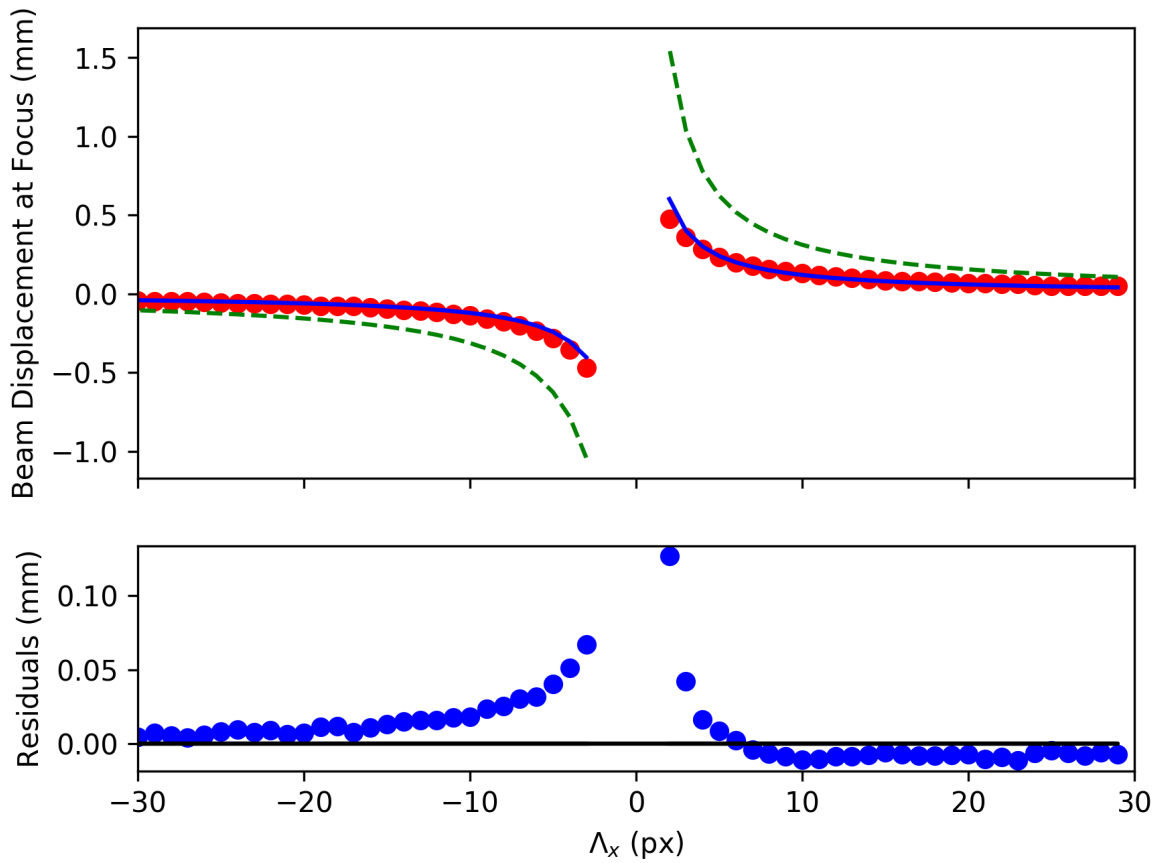


Figure 2.5: The plot shows the beam displacement as a function of the width of the blazed grating (Λ_x) and the residuals between the fit points and raw data. The dashed lines show the plot of the theoretical values computed from Equation 2.2.2 with $k = 3.12\text{mm} \cdot \text{px}$, the dots is the plot of the raw data, while the solid line is the best fit of raw data.

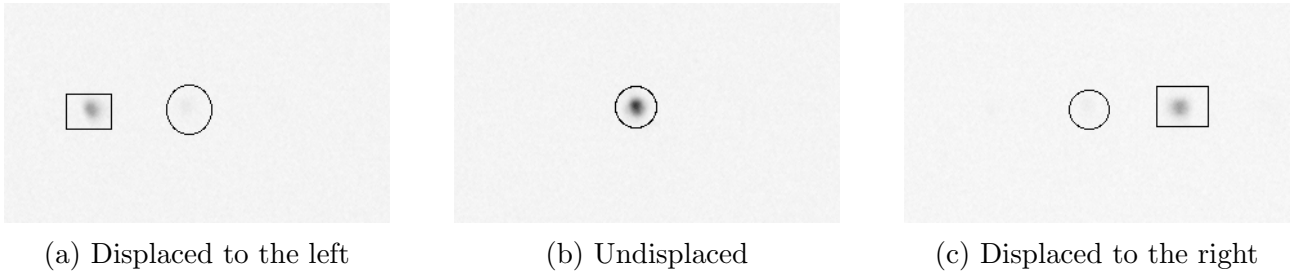


Figure 2.6: Negatives of some images captured in the beam displacement measurement. The positions of the beam are highlighted by the rectangles. As there is some faint remnants of vertically polarised light (which remains undisplaced as they are not affected by the phase shifts), we highlight the spots showing where the original positions were with the circles to illustrate the displacement of the beam

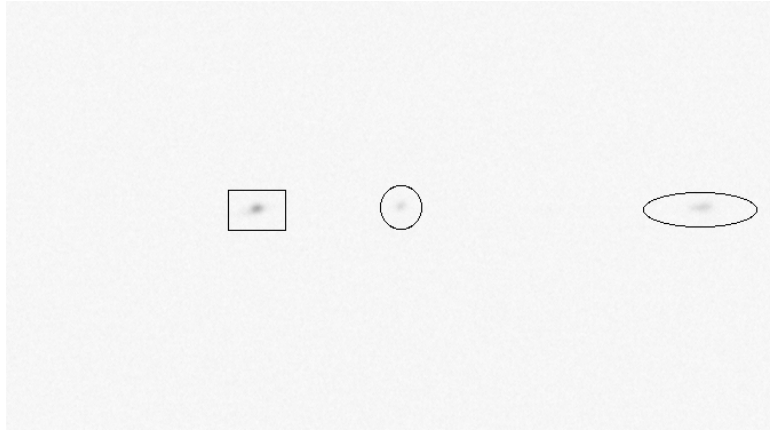


Figure 2.7: A negative image captured on the camera for a pattern with a small Λ_x . The rectangle highlights the beam that is displaced to the intended position, whereas the ellipse highlights the beam that is unintentionally displaced. The circle in the center is the faint remnant of the vertically polarised light as explained in Figure 2.6

periodicity Λ_x , a part of the beam is displaced in the direction opposite to where it was intended (Figure 2.7). This is attributed to the poor resolution of the phase shift patterns as the changes in phase shift between each pixel become very sharp. Hence, sharp phase shifts between pixels should be avoided.

2.3 Beam Position Measurements

Working towards our goal of correcting the wavefront of a light beam, there is a need to find the position of the beam that is incident on the SLM. This is due to the need to implement phase shifts that are polar functions that centers about the center of the beam. We developed 2 methods that use the SLM to determine which pixel on the SLM the beam is centered about.

2.3.1 Method A: Using the birefringence of the SLM

This method exploits the birefringence of the SLM to find the location of the beam and make use of the same setup for characterising the phase shifts on the SLM (Figure 2.1). With the results obtained from Section 2.1, we determine the amount of phase shift that gives maximum transmitted intensity (ϕ_{\max}) and the phase shift that gives the minimum transmitted intensity (ϕ_{\min}) detected in D1. We then proceed to find the X-position of the beam on the SLM.

First, we create an image of a vertical bar of width d pixels using ϕ_{\max} , with the left edge of this bar aligned to the left edge of the SLM array. This bar is overlaid on a background of ϕ_{\min} (as shown in Figure 2.8). We then upload this image with the appropriate post processing and record the intensity of light at detector D1. After the measurement, we create a new image by move the vertical bar by d pixels to the left while keeping the width of the bar constant at d . We upload this new image after post processing and record the intensity measurement at D1 again. This repeats until the right edge of the bar reaches the right edge of the SLM. We then find the position of the left edge of the bar that gives the maximum transmission intensity (px_{\max}), and repeat the measurement in the region around px_{\max} using a bar with a smaller width d to fine tune into the position of px_{\max} . This measurement is repeated with a horizontal bar for the Y-position of the beam. Examples of the data collected during the scans are plotted in Figure 2.9

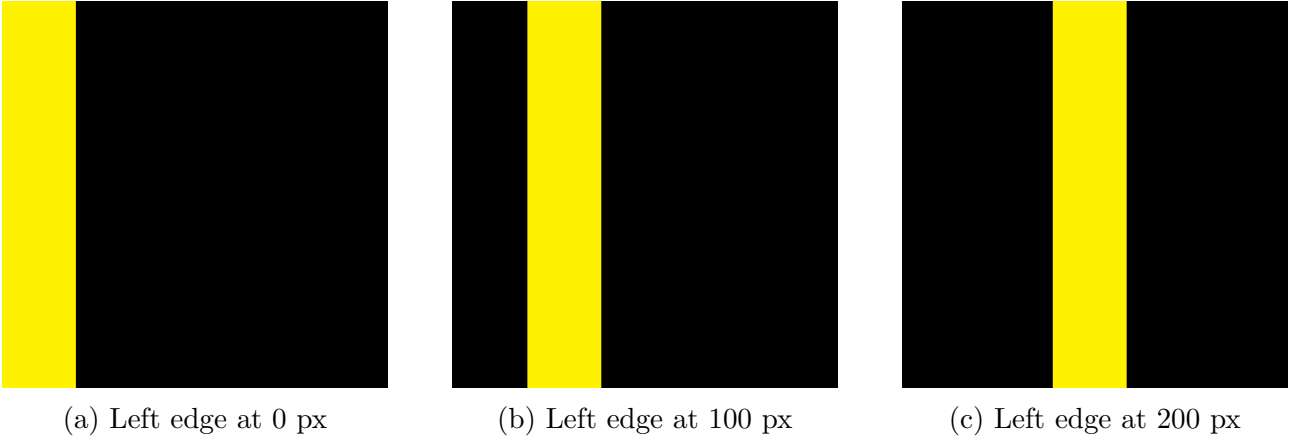


Figure 2.8: The above 3 figures shows successive images that was used to scan for px_{\max} (without the wavefront correction). For illustrative purposes, ϕ_{\min} is represented as black and ϕ_{\max} is represented as yellow. Each of these yellow bars is 100 pixels in width ($d = 100$)

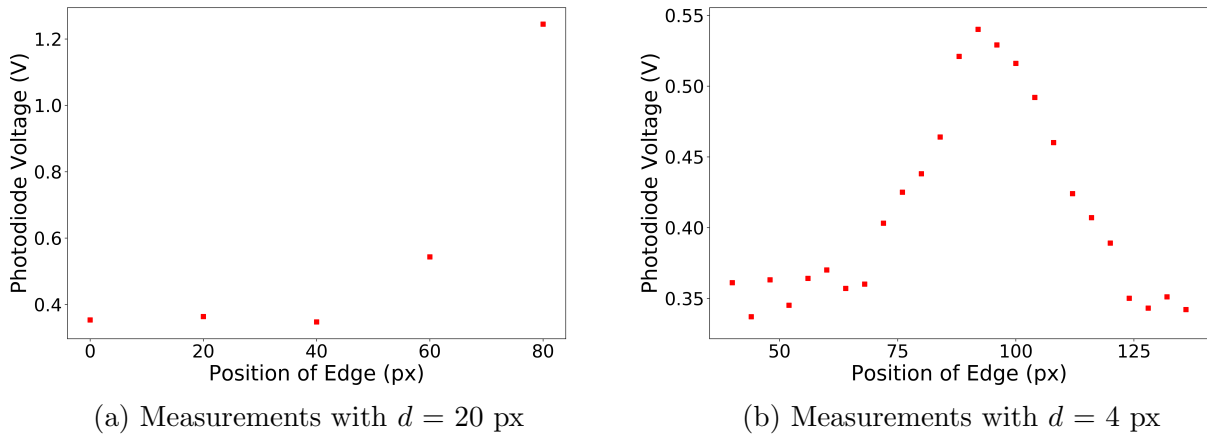


Figure 2.9: The above 2 figures shows the data obtained in two successive scans (different d) for px_{\max} in the Y-direction. Note that we used a photodiode for the light intensity measurement. The voltage across the resistor in the photodiode (the vertical axes in the plots) is propotional to the intensity of light. The use of a smaller d also reduces the intensity of light at the detector.

The method that I have just described has the downsides of having to use additional optical components in order to do the measurement, which is removed after the measurements to locate the position such that the beam incident on the SLM is horizontally polarised. This need to remove and replace the halfwave plates is difficult if they are situated in inaccessible places of our setup. Furthermore, the removal of the waveplate before the SLM may change the position of the beam on the SLM. Hence, an alternative method that is less invasive to the setup is

needed.

2.3.2 Method B: Fashioning the SLM as a Knife Edge

A knife edge measurement is a method to measure the width of a beam by intentionally clipping a beam using a razor blade, and measuring the intensity of the clipped beam with respect to the position of the razor blade. Similar to how a knife edge obstructs the transmission of light, we use a random phase shift on the SLM to scatter part of the light incident on the SLM. We quantify the amount of light that is scattered by measuring the output intensity of the light that is coupled into an optical fiber after it is reflected off the SLM.

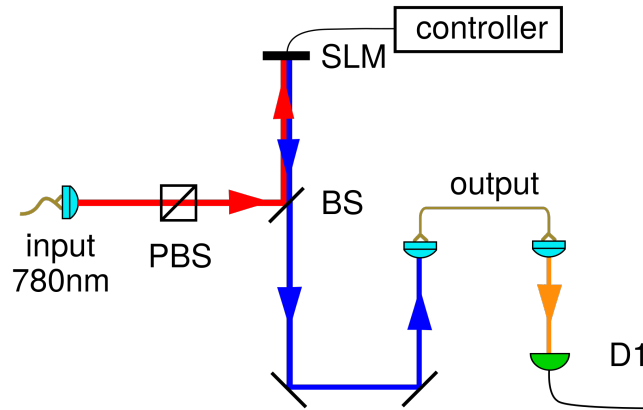
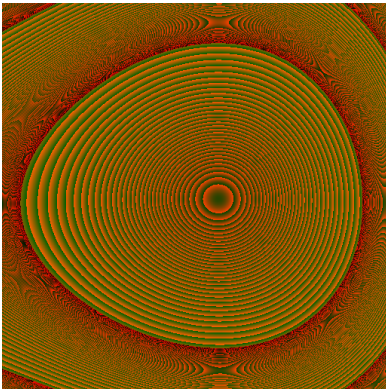


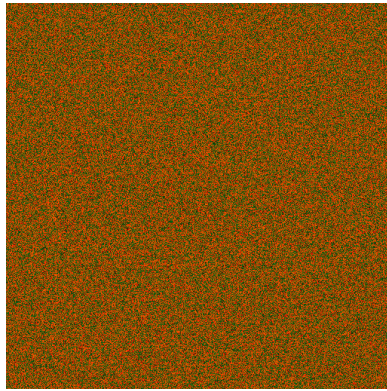
Figure 2.10: Simplified setup to measure beam position and size on the SLM

In order to find the X-position of the beam on the SLM, we start by measuring output light intensity from the fiber (D1) when a zero-phase shift image is uploaded (I_0). We proceed to upload an image that is completely filled with random phases overlaid on top of the zero-phase shift image, and measure the output light intensity from the fiber (I_1). We “reveal the beam” by removing part of the random phase shift image that overlays the zero-phase shift image from the left of the SLM, and measure the resultant I_1 . Figure 2.11 illustrates the process.

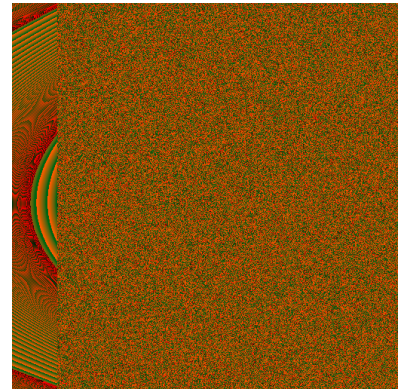
The ratio of I_1 divided by I_0 , which we term the improvement ratio (γ), is calculated, and a fit to following function is done:



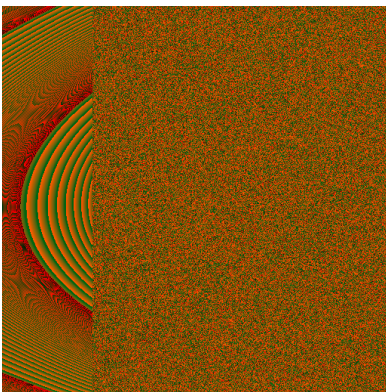
(a) Measuring I_0



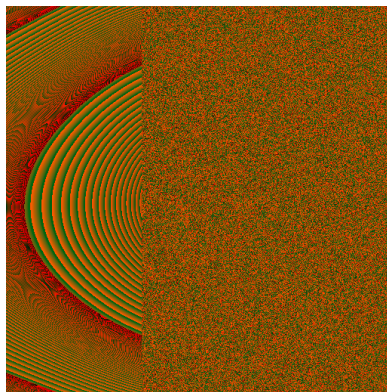
(b) “Covering” up the whole beam



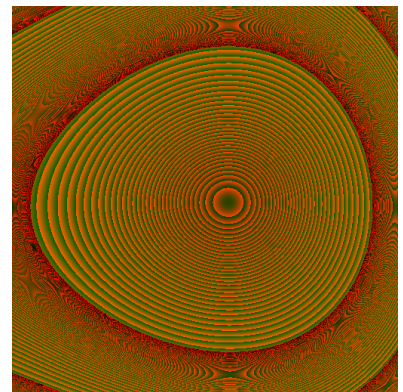
(c) “Revealing” up to 60 pixels



(d) “Revealing” up to 120 pixels



(e) “Revealing” up to 180 pixels



(f) Fully “revealing” the beam

Figure 2.11: The above 6 figures shows the postprocessed image uploaded to our SLM in order of how the measurements were done. (a) was used for our measurement of I_0 while (b)-(f) was used to measure I_1 . Note: The amount we “reveal” per subsequent measurement is actually smaller as the above images were chosen to make the “revealing” process more obvious to the reader.

$$\gamma(x) = \frac{1}{2} \left(1 + \operatorname{erf} \left(\frac{x - \mu}{\sigma} \right) \right) \quad (2.3.1)$$

where erf is the Error-function, x is the position on the SLM where the random phase shifts starts, μ is the center of the beam on the SLM, and σ is a variable that relates to the beam waist.

Figure 2.12 shows an example of the plot of the data points and the fit to Equation 2.3.1 with the free parameters μ and σ . From the μ and σ , we are able to obtain the X-position of the center of the beam and the beam waist. This process is repeated for the Y-direction but the beam is “revealed” upwards instead.

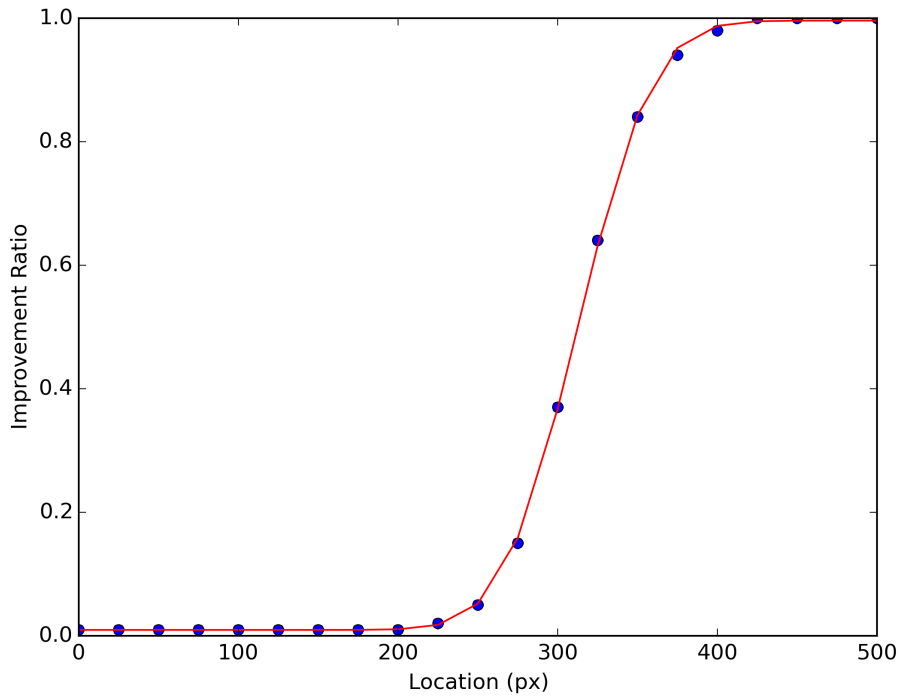


Figure 2.12: A plot from the data to measure the X position of the beam. The blue dots shows the raw data that was measured and the red line is the interpolation of the best fit values. From the fit function, the center position along the X direction of this beam is found to be at 312.8 ± 0.3 pixels and the beam waist is 73.3 ± 0.9 pixels.

In comparison to the method described in Subsection 2.3.1, this method has few benefits.

First, it removes the need to replace the optical components into the setup whenever we want to find the position of the beam on the SLM. Second, not only are we able to locate the beam, but at the same time we are able to find the beam waist of the beam on the SLM.

2.4 Creating Laguerre-Gaussian Mode Beams

Next, we apply more complex phase shift patterns that have azimuthal dependence, in particular, using the SLM to create Laguerre-Gaussian mode beams from a regular Gaussian beam. Laguerre-Gaussian mode beams are sometimes called “donut” beams, as the image of these beams, when viewed at the focal plane of a converging lens, appears like a ring. The phase relation (Φ_m) for a monochromatic Laguerre-Gaussian mode beam can be described by the following equation [13]:

$$\Phi_m(r, \theta, z) = [u(r, z) e^{ikz}] \cdot (e^{im\theta}) \quad (2.4.1)$$

where r, θ, z are the cylindrical co-ordinates of the beam propagating along the z -axis, k is the wavenumber of the light in the beam, and u is the wave profile of the light at position r, z , and m is an index known as the topological charge which essentially quantifies how “twisted” the Laguerre-Gaussian mode is.

Applying Equation 2.4.1 to our construct of the experiment, the term $[u(r, z) e^{ikz}]$ describes our Gaussian beam that is sent to the SLM, whereas the term $(e^{im\theta})$ transforms our Gaussian beam into a Laguerre-Gaussian mode with topological charge m . Hence, we apply a Laguerre-Gaussian phase shift pattern on the SLM for the transformation. The range of phase shift theoretically required for the helix is in the range $[0, 2m\pi]$. However, since the phase shift is periodic every 2π and we are limited by the working range of the SLM, we take perform a modulus 2π on the phase shift required. This results in the phase shift that we upload having m number of helices on it. The sign of m also determines the handedness of the helix. This

equation for the phase shift to be performed on the SLM is therefore:

$$\phi_m(\theta) = m\theta \quad (2.4.2)$$

where ϕ_m is the phase shift pattern to create the a Laguerre-Gaussian beam with topological charge m in the polar co-ordinate system centered about the center of the beam on the SLM.

A visualisation of how the phase shift pattern uploaded to the SLM for some positive and negative values of m is shown in Figure 2.13.

We assemble the setup in the same manner as Figure 2.4. We use methods described in Section 2.3 to locate the center of the beam. We capture in a video ¹ the way the beam profile changes with phase shift patterns of different m in Equation 2.4.2. Screenshots of what was observed and the simulated images is shown in Table 2.1. Although the expected trend of the rings becoming thinner and larger in radius with increasing m was observed in the screenshots, further investigation to check radius of the rings matches the predicted values has to be done.

¹The video can be viewed on: <https://youtu.be/rMRvlee5wuU>

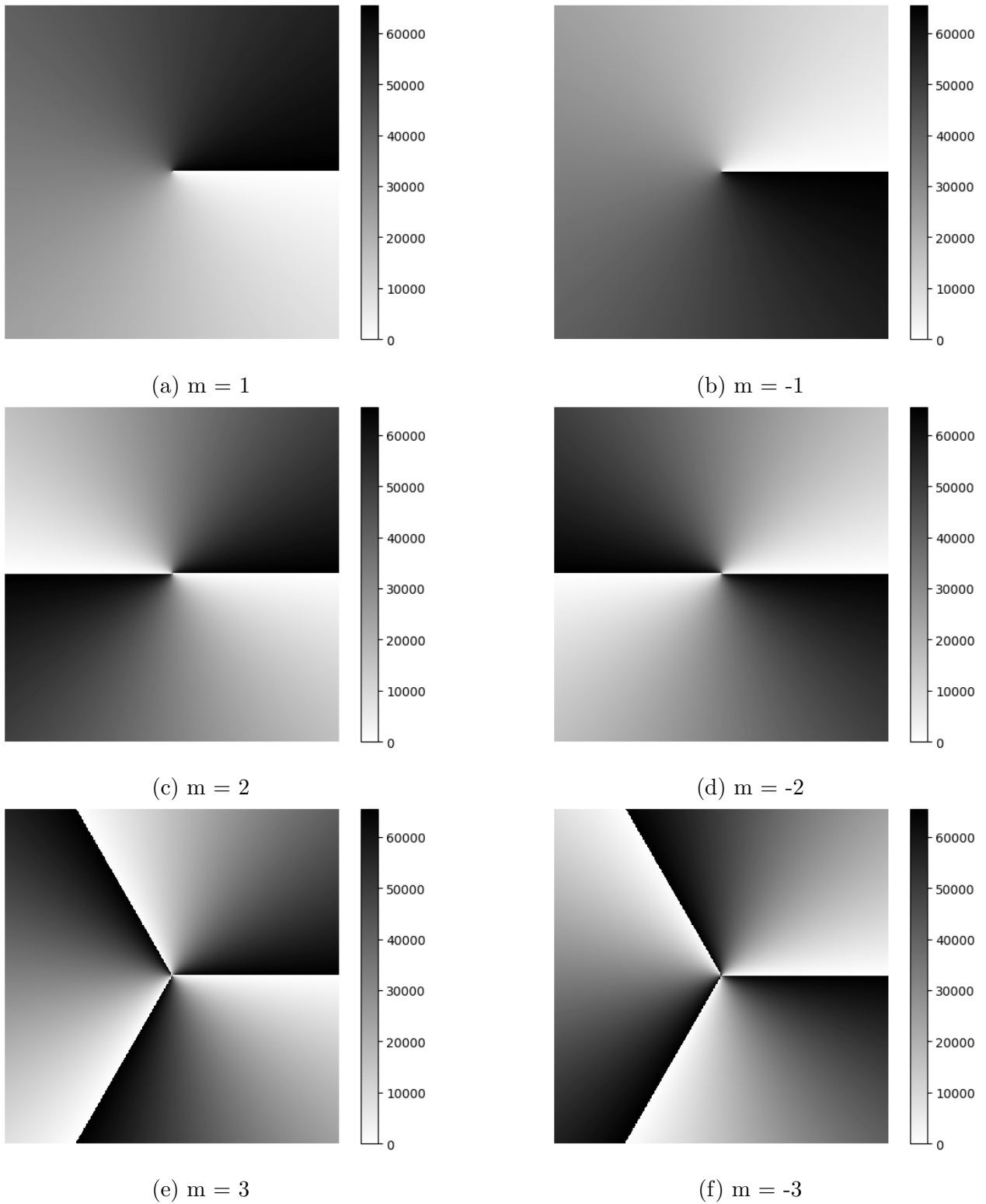


Figure 2.13: Visualisation of phase shift patterns uploaded to the SLM (shown without the wavefront correction image) for a beam which has a center at the center of the SLM. The heatmap shows the amount of phase shift in terms of the pixel value (0 - 65535). The patterns on the left column give handed phase shifts, and the patterns in the right column gives left handed phase shifts. The number of helices increases down the rows.

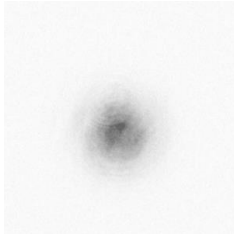
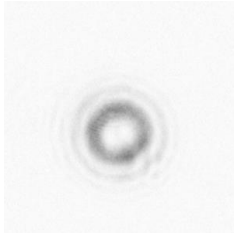
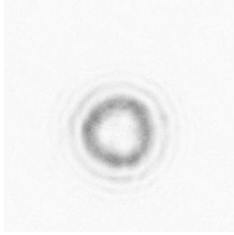
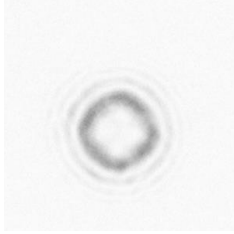
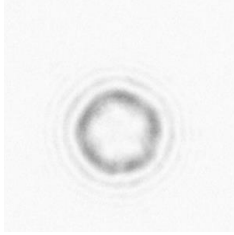
m	Simulation	Screenshot
0		
1		
2		
3		
4		

Table 2.1: A table of the simulation and screenshot of the image for the performed phase shifts in Equation 2.4.2 for different n .

Chapter 3

Measuring Wavefronts

Since we are interested in correcting the wavefronts of light, there is a need for a method to measure these wavefronts and quantify them somehow. In this chapter, we shall discuss the device known as the Hartmann-Shack wavefront sensor that we use to measure the wavefront of the light, as well as how we quantify the wavefronts using Zernike modes.

3.1 Hartmann-Shack Wavefront Sensor

The device that we use to measure the wavefront of light is called the Hartmann-Shack wavefront sensor. This wavefront sensor makes use of an array of converging micro-lenses (also called lenslets) attached to a CCD camera in order to measure the wavefront of light. Figure 3.1 shows how the lenslet array attachment looks like.



Figure 3.1: A photograph of the lenslet array that can be affixed onto the CCD camera. The green dots on the optical element is the lenslet array reflecting the lighting in the laboratory

3.1.1 How it Works

In ray optics, if a beam that is parallel to the optical axis is shone onto a converging lens, the focal point of the beam is where the focal plane meets the optical axis. However, if the beam is shone onto the converging lens at an angle, the focal point of this beam no longer lies on the optical axis. This displacement of the focal point can be used to determine the direction of approach of the beam. The wavefront of light can be broken down into small planar wavelets that approaches each micro-lens on the lenslet array. If the wavefront is not planar, each wavelets approaches each lens from a different direction. This in turn causes the focal point of the beam shone onto each lenslet to be displaced on the focal plane. A pictorial description of the above is shown in Figure 3.2

The CCD camera then notes the positions of the focal point for each lenslet on the lenslet array. The information of the displacement of the focal points are processed to reconstruct the wavefront of the light.

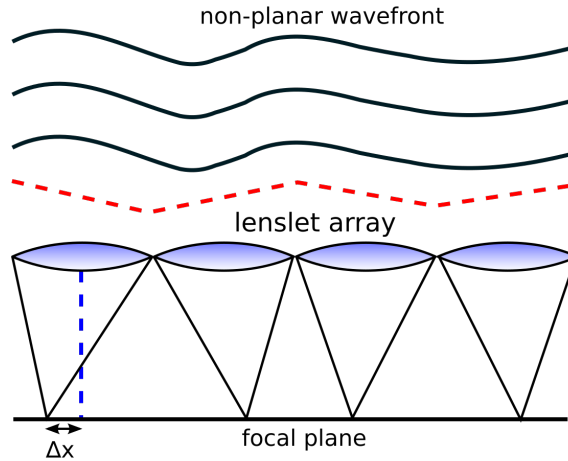


Figure 3.2: The above diagram shows how the a non-planar wavefront is focused on with an array of lenslets. Shown earlier in Figure 2.3, a beam that propagates at angle towards a lens creates a displacement of the focal point on the focal plane. A non-planar wavefront is deconstructed into wavelets that approach each lenslet at an angle, resulting in the displacement of the beam spot by Δx from its original focal point (the intersection of the blue dotted line and the focal plane). The red dotted line shows the deconstruction of the non-planar wavefront (black lines) to planar wavelets [14].

3.1.2 A Note on the Lenslet Array

A drawback on the wavefront sensor is that the reconstructed wavefront is obtained from the information after discretising the wavefront into wavelets incident on the lenslet array. Hence, we can only obtain as many data points as there are lenslets on the array.

This is a consideration when choosing which lenslet array we affix onto the CCD camera. If we were to use a an array with more lenslets, this means that we are able to obtain more data points for the reconstruction of the wavefront. However, this also means that the resolution of the focal point's displacement is reduced as there are now less pixels on the CCD camera dedicated to each lenslet to determine the displacement of the focal point.

On the other hand, if we were to use an array with less lenslets, the resolution of the focal point's displacement increases, but at the same time, the number of data points we have to reconstruct the wave is reduced.

3.2 Zernike Modes

The wavefront of light can be decomposed via a polynomial basis and the common choice for this basis are the Zernike modes. The Zernike modes or Zernike polynomials forms a basis of polynomials that are orthogonal on a unit disk. In Noll's index, the Zernike modes are described by the following equation [15]:

$$Z_n^m(r, \theta) = \begin{cases} R_n^m(r) \cos(m\theta) & , \text{ even } m \\ R_n^m(r) \sin(m\theta) & , \text{ odd } m \end{cases}$$

$$R_n^m(r) = \begin{cases} \sum_{k=0}^{\frac{n-m}{2}} \frac{(-1)^k (n-k)!}{k! (\frac{n+m}{2}-k)! (\frac{n-m}{2}-k)!} r^{n-2k} & , \text{ even } n-m \\ 0 & , \text{ odd } n-m \end{cases}$$

where m and n are the Noll's indices for the Zernike mode and $r \in [0, 1]$ is the normalised radial co-ordinates and θ is the azimuthal co-ordinates. A mapping between the mode number and Noll index is achieved via OEIS sequence A176988 [16].

The reason why these set of polynomials are commonly used in optics is because these polynomials are closely related to typical optical aberrations. For example, vertical astigmatism, the aberration on the lens when the focus of the rays that propagate horizontally to the optical table and focus of the rays propagating vertically to the optical tables are at a different positions, can be described by Zernike mode Z_2^2 . As we intend to correct for lens aberrations, we can use Zernike modes to form a basis for our phase shifts. A table showing information about the first 6 Zernike modes can be seen in Table 3.1.

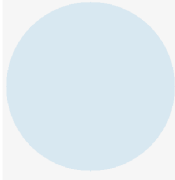
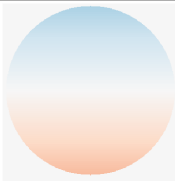
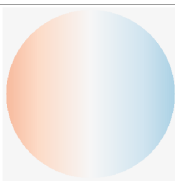
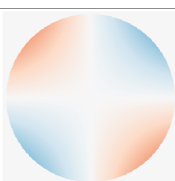
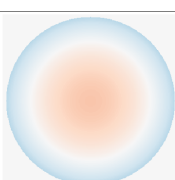
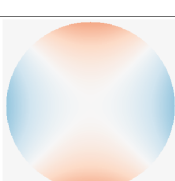
Mode No.	Noll Index (n, m)	Equation	Abberation Name	Phase Shift Visualisation
1	0,0	1	Piston	
2	1,-1	$2r \sin \theta$	Vertical Tilt	
3	1,1	$2r \cos \theta$	Horizontal Tilt	
4	2,-2	$\sqrt{6}r^2 \sin 2\theta$	Oblique Astigmatism	
5	2,0	$3(2r^2 - 1)$	Defocus	
6	2,2	$\sqrt{6}r^2 \cos 2\theta$	Vertical Astigmatism	

Table 3.1: A table of the first 6 Zernike modes with their respective equations, aberration names, and phase shift visualisation shown. The blue regions represents positive phase shifts while red regions represent negative phase shifts with the intensity of the colours proportional to the magnitude of the phase shifts.

Chapter 4

Effect of Wavefront Corrections on Fiber Coupling

Preliminary to coupling light to an atom, we conduct a test to see whether wavefront corrections to a beam can improve the coupling of light to a monomode optical fiber.

In order to send light through an optical fiber, we have to attain send light into an optical fiber in the reverse manner of how light emerges from the optical fiber, which means the light has to match the mode of the optical fiber. This requires the light to enter the optical fiber with the correct convergence (via a lens in the coupler) and direction. Not all the light that is sent to the fiber satisfies the above condition and hence only some part of the light is able to enter the fiber. The part of light that is transmitted through the fiber is said to be coupled into the fiber. We define the coupling efficiency (η) to be the ratio of the intensity of light that comes out of an optical fiber to the intensity of light that we send to it.

First, we benchmark the optical fiber with the setup shown in Figure 4.1. By measuring the intensity of light that enters the optical fiber labelled output and the intensity of light measured at detector D2, we benchmark the maximal coupling efficiency when the light is reflected off a mirror (M1) instead of an SLM to be 86%.

We modify the setup in Figure 4.1 to the setup seen in Figure 4.2. In comparison to setups

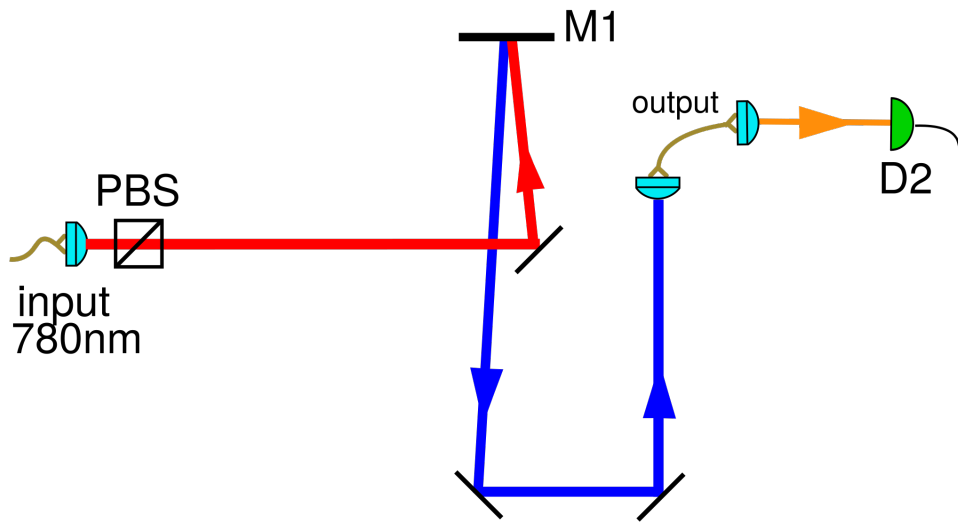


Figure 4.1: Setup to benchmark the optical fiber

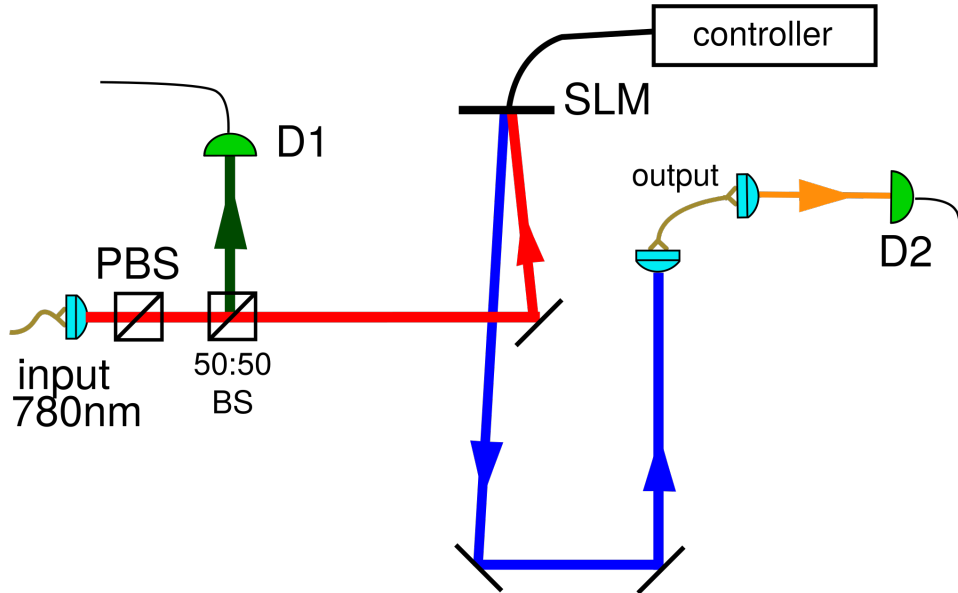


Figure 4.2: Experimental setup using the SLM. Compared to Figure 4.1, the mirror M1 is replaced with the SLM and an additional 50:50 beam splitter is added to measure the input light intensity.

used for the experiments described in the Chapter 2, we use a mirror to divert the light to the SLM at a small incidence angle instead of a beam splitter as we do not want a drop in the intensity of light going to the SLM. The small angle is to ensure that light that enters each pixel on the SLM is backreflected through the same pixel.

We measure the intensity of light at detector D1 (I_0) and the intensity of light before it enters the output fiber (I_{in}) when a zero-phase shift image is uploaded. Subsequently, we only measure the intensity of light at detector D1 (I_1) and at detector D2 (I_{out}). The coupling efficiency is computed in the following manner:

$$\eta = \frac{I_{in}}{I_0} \cdot \frac{I_1}{I_{out}} \quad (4.0.1)$$

where the values of I_{in} and I_0 is kept constant.

After assembling the setup, we use the method in Subsection 2.3.2 to find the position and beam waist of the incident beam on the SLM. We attempt to improve the coupling efficiency by applying a phase shift pattern ($\phi(r, \theta)$) by superposing Zernike modes (Z_n) that are centered about the beam's center on the SLM, with the radius of the disk normalised to a factor of r_0 , each multiplied by with coefficient (c_n):

$$\phi(r, \theta) = \sum_1^m c_n Z_j \left(\frac{r}{r_0}, \theta \right) \quad (4.0.2)$$

where m is the number of Zernike modes we are using, Z_j being the j -th Zernike mode, r is the radial co-ordinates centered about the beam center on the SLM and θ is the azimuthal co-ordinates.

We initialised all values of c_n in Equation 4.0.2 to 0. Starting with the first Zernike mode ($n = 1$), we measure the coupling efficiency by varying the value of c_1 , and perform a fitting the data points to a parabolic curve to find the optimal value of c_1 that gives the maximum coupling efficiency. We set the value of c_1 in Equation 4.0.2 to this optimal value. We proceed to $n = 2$ and get the optimal value of c_2 in a similar method to how we obtained c_1 , while

keeping all other values of c_n constant. An example of the plot of the data in the process of optimising c_n can be seen in Figure 4.3. This process is repeated until we reach $n = m$ and we repeat this whole process again starting from $n = 1$ without reinitialising all the values of c_n to 0. We scan through 3 cycles of the Zernike modes. We performed the above optimisation process for different values of normalising radius r_0 as shown in Figure 4.4.

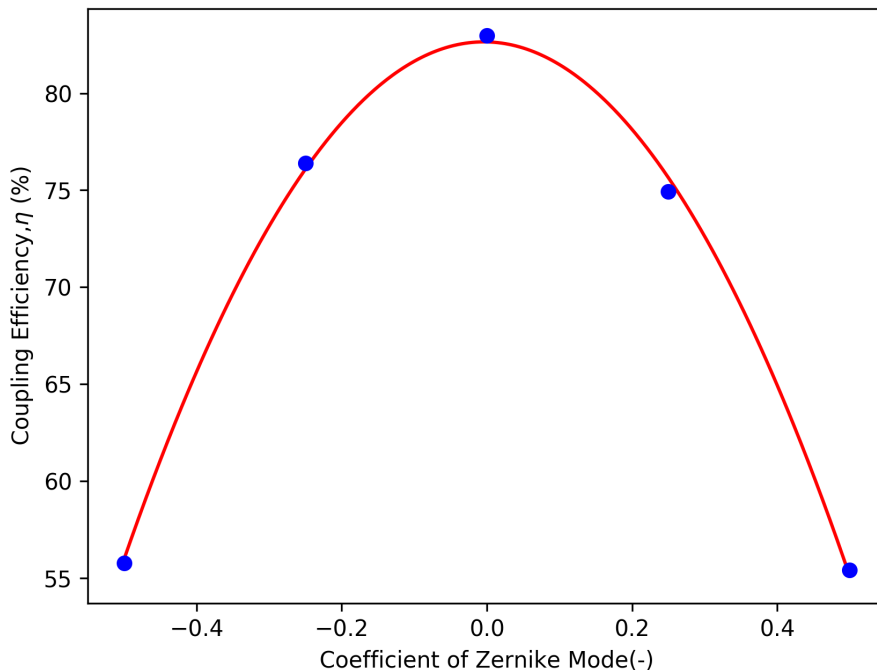
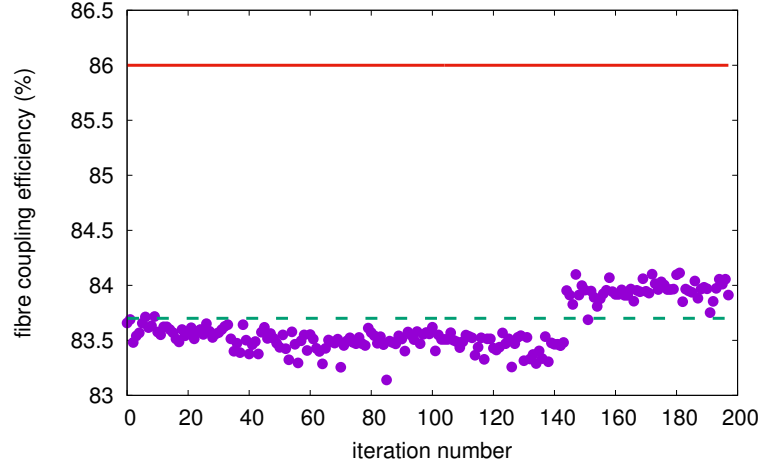
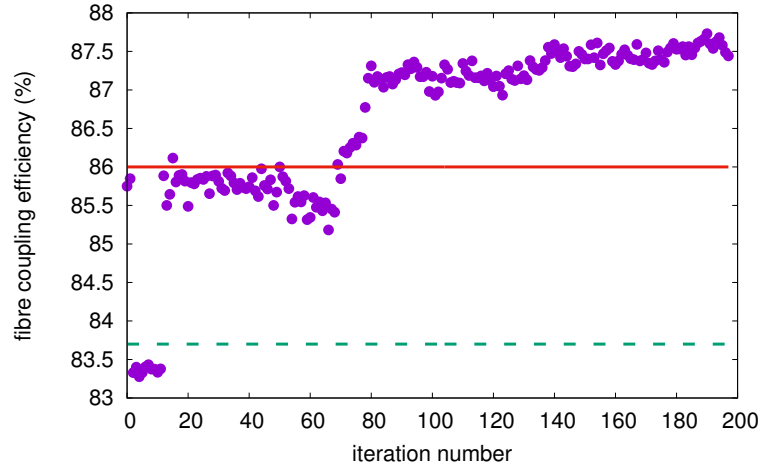


Figure 4.3: A example of the plot of data points to find the coefficient for the Zernike modes. The blue dots show the values obtained from measurement whereas the red lines are the interpolation of values obtained from the fit.

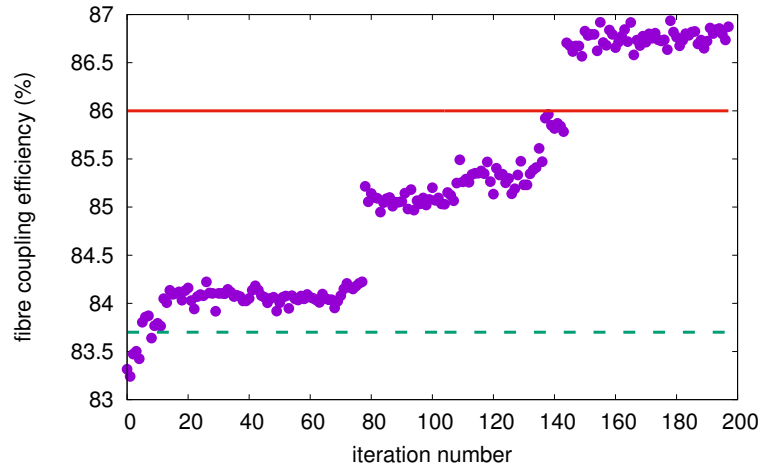
From the scans performed, we note that the optimisation process does not work well when the normalising radius r_0 is the size of the beam waist on the SLM, as the maximum coupling efficiency is worse off than that when a mirror is used (Figure 4.4a). On the other hand, when r_0 is 2 or more times larger than the beam waist, we see that the coupling efficiency can surpass the coupling efficiency when we use the mirror. Hence, the value of r_0 has to be at least 2 times larger than the beam waist in order for the optimisation process to be effective. When r_0 is sufficiently large, we are able to correct the wavefront successfully as the maximum coupling



(a) $r_0 = 39$ pixels



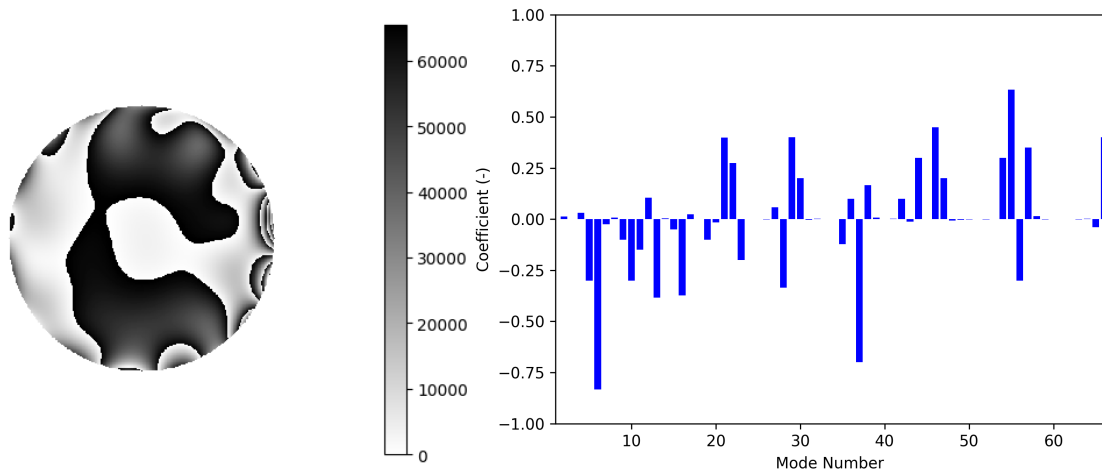
(b) $r_0 = 78$ pixels



(c) $r_0 = 117$ pixels

Figure 4.4: The above 3 figures show the progression of the output fiber coupling efficiency through the course of the optimisation process for different values of normalising radius (r_0) for a beam with a beam waist of 39 pixels on the SLM. The solid line is the coupling efficiency we obtained when using a mirror and the dashed line shows the coupling efficiency when a zero-phase shift image is uploaded on the SLM. For the scan, we use 66 Zernike modes ($m = 66$). The iteration number is obtained by $66(\text{cycle number}) + n - 1$ where n is the index for the Zernike mode optimised in that iteration.

efficiency is better than the coupling efficiency when a mirror is used. A visualisation of a phase shift that produces the optimal coupling efficiency from one of our scans is shown in Figure 4.5a.



(a) Visualisation of phase shift

(b) Zernike modes coefficient.

Figure 4.5: (a) shows the visualisation of the phase shift which gives the optimal coupling efficiency. (b) is the shows the amplitudes of the coefficients for the Zernike modes that makes up the phase shift in (a)

We also note that the maximum coupling efficiency achieved decreases slightly when the normalising radius (r_0) gets too large (comparing r_0 2 times larger than the beam waist to when it is 3 times larger). This is because the main features in some of the higher order Zernike modes are more significant nearer to the circumference of the unit disk. Hence, if r_0 is too large, these features would be too far from the center of the beam to take significant effects.

Chapter 5

Conclusion

We began this report by introducing the SLM, explaining the technical details on how the SLM works in Chapter 1. In Chapter 2, we discussed some of the experiments conducted in order to familiarise with the SLM, with most of the results we obtained were as predicted. We introduced the Hartmann-Shack Sensor and Zernike modes in Chapter 3, which set the stage for the experiment on improving the coupling efficiency for Chapter 4. We have demonstrated success in correcting the wavefront by obtaining an improved coupling efficiency.

5.1 Future Outlook

We have to conduct further investigations to find the source of discrepancy in the theoretical values and calculated values for some of the experiments.

Despite understanding the function of the Hartmann-Shack sensor, we unfortunately did not have the opportunity to use the device as an active component to our setup due to software limitations. We hope to incorporate the sensor into our future experiments.

Lastly, we would also like to conduct further investigations on how else changes to the wavefront affects beam parameters, such as the beam waist, as well as further the study on how the wavefront affects the interaction between light and the atom.

Bibliography

- [1] J. I. Cirac, P. Zoller, H. J. Kimble, and H. Mabuchi. Quantum state transfer and entanglement distribution among distant nodes in a quantum network. *Phys. Rev. Lett.*, 78:3221–3224, Apr 1997.
- [2] L-M Duan, MD Lukin, J Ignacio Cirac, and Peter Zoller. Long-distance quantum communication with atomic ensembles and linear optics. *Nature*, 414(6862):413–418, 2001.
- [3] Yimin Wang, Ji ří Minář, Lana Sheridan, and Valerio Scarani. Efficient excitation of a two-level atom by a single photon in a propagating mode. *Phys. Rev. A*, 83:063842, Jun 2011.
- [4] Eustace L. Dereniak and Teresa D. Dereniak. *Aberrations in optical systems*, page 292–327. Cambridge University Press, 2008.
- [5] Meng Khoon Tey, Zilong Chen, Syed Abdullah Aljunid, Brenda Chng, Florian Huber, Gleb Maslennikov, and Christian Kurtsiefer. Strong interaction between light and a single trapped atom without the need for a cavity. *Nature Physics*, 4(12):924–927, 2008.
- [6] Larry J Hornbeck. Deformable-mirror spatial light modulators. In *Proc. SPIE*, volume 1150, pages 86–102, 1989.
- [7] Gordon D Love. Wave-front correction and production of zernike modes with a liquid-crystal spatial light modulator. *Applied optics*, 36(7):1517–1524, 1997.

- [8] Selam Ahderom, Mherdad Raisi, Kungmang Lo, Kamal E Alameh, and Rafie Mavaddat. Applications of liquid crystal spatial light modulators in optical communications. In *High Speed Networks and Multimedia Communications 5th IEEE International Conference on*, pages 239–242. IEEE, 2002.
- [9] Inc. Meadowlark Optics. *HV 512 SLM-DVI - User Manual*. Meadowlark Optics, Inc.
- [10] James A Rego, Jamie AA Harvey, Andrew L MacKinnon, and Elysse Gatdula. Asymmetric synthesis of a highly soluble ‘trimeric’ analogue of the chiral nematic liquid crystal twist agent merck s1011. *Liquid crystals*, 37(1):37–43, 2009.
- [11] Fanghong Li, Naohisa Mukohzaka, Narihiro Yoshida, Yasunori Igasaki, Haruyoshi Toyoda, Takashi Inoue, Yuji Kobayashi, and Tsutomu Hara. Phase modulation characteristics analysis of optically-addressed parallel-aligned nematic liquid crystal phase-only spatial light modulator combined with a liquid crystal display. *Optical review*, 5(3):174–178, 1998.
- [12] *Large 512 X 512 Spatial Light Modulator*. Meadowlark Optics, Inc.
- [13] Jennifer E. Curtis and David G. Grier. Structure of optical vortices. *Phys. Rev. Lett.*, 90:133901, Apr 2003.
- [14] Shack Hartmann WFS Lenslet Array, 2pem,
https://commons.wikimedia.org/wiki/File:Shack_Hartmann_WFS_lensletarray.svg.
- [15] Robert J Noll. Zernike polynomials and atmospheric turbulence. *JOSA*, 66(3):207–211, 1976.
- [16] OEIS Sequence A176988, <https://oeis.org/A176988>.